



Lensfree on-chip microscopy based on single-plane phase retrieval

CHENG GUO,^{1,2,3,7} XIANMING LIU,³ FEILONG ZHANG,³ ,
YONGBIN DU,^{1,2} SHENGHAO ZHENG,^{1,2} ZEHUA WANG,^{1,2}
XIAOQING ZHANG,⁴ XINGCHI KAN,⁵ ZHENGJUN LIU,⁶ ,
AND WEIBO WANG^{1,2,8}

¹Center of Ultra-precision Optoelectronic Instrument Engineering, Harbin Institute of Technology, Harbin 150080, China

²Key Lab of Ultra-precision Intelligent Instrumentation (Harbin Institute of Technology), Ministry of Industry and Information Technology, Harbin 150080, China

³School of Computer Science and Technology, Harbin Institute of Technology, Harbin 150001, China

⁴School of Life Science and Technology, Harbin Institute of Technology, Harbin 150080, China

⁵College of Veterinary Medicine, Jilin University, Changchun 130062, China

⁶School of Physics, Harbin Institute of Technology, Harbin 150001, China

⁷guocheng_27@163.com

⁸wwbhit@hit.edu.cn

Abstract: We propose a novel single-plane phase retrieval method to realize high-quality sample reconstruction for lensfree on-chip microscopy. In our method, complex wavefield reconstruction is modeled as a quadratic minimization problem, where total variation and joint denoising regularization are designed to keep a balance of artifact removal and resolution enhancement. In experiment, we built a 3D-printed field-portable platform to validate the imaging performance of our method, where resolution chart, dynamic target, transparent cell, polystyrene beads, and stained tissue sections are employed for the imaging test. Compared to state-of-the-art methods, our method eliminates image degradation and obtains a higher imaging resolution. Different from multi-wavelength or multi-height phase retrieval methods, our method only utilizes a single-frame intensity data record to accomplish high-fidelity reconstruction of different samples, which contributes a simple, robust, and data-efficient solution to design a resource-limited lensfree on-chip microscope. We believe that it will become a useful tool for telemedicine and point-of-care application.

© 2022 Optica Publishing Group under the terms of the [Optica Open Access Publishing Agreement](#)

1. Introduction

Lensfree on-chip microscopy [1–3] provides a solution to image an object with high resolution (~ 500 nm) and large field-of-view ($\geq 20\text{mm}^2$), since the present CMOS sensor chip has a small pixel size and large pixel counts. Till now, lensfree imaging modality has evolved into a series of portable platforms in the application of digital pathology [4,5], microfluidic device [6,7], environment monitoring [8], and cell culture [9,10]. Lensfree on-chip microscope originates from Gabor's digital in-line holography system [11,12], where scattered light from a sample interferes with unscattered background to form a hologram (or intensity) on the sensor. The recorded holograms are post-processed by a computer to reconstruct the transmitted wave field of the sample. The core point of lensfree image reconstruction lies in how to remove the twin-image and self-interference artifacts without resolution loss and image degradation. To address it, many lensfree imaging methods have been proposed, including multispectral scanning [13–15], multi-angle illumination [16,17], multi-height measurement [18–22], coding mask modulation [23,24], off-axis reflection configuration [25], and ptychographical scanning [26,27]. The above methods increase the experimental complexity or physical constraint to measure multi-frame

intensity images. From a perspective of compact design, a potential demand of lensfree on-chip microscope is to dispense with extra optical-mechanical components but only use a single-frame intensity image to accomplish high fidelity recovery of different samples.

To realize single-frame image reconstruction, many computational approaches have been investigated. The common methods utilized a double-side constrained phase retrieval framework [28–36], where the shape of object (referred to support region) and the square root of recorded intensity image were enforced as object and observation constraints at each iteration. Among them, image segmentation [28–30], L1 regularization [31,32], and shrink-wrapping strategy [33–36] have been used to extract the support region. But the support-based methods are only suitable for isolated or sparse samples. R. Horisaki et al [37,38] inserted a random binary mask between sample and sensor planes to form a coding imaging system, where transmitted functions of the mask and sample planes can be jointly reconstructed by Gerchberg-Saxton algorithm [39] and sparse optimization [40]. Without the coding mask, L. Cao et al [41] modeled single-frame holographic recovery as a compressive sensing task in gradient domain and solved it by a two-step iterative shrinkage thresholding method. Nevertheless, the required sparse assumption of compressive sensing is difficult to be satisfied for dense samples, such as pathological slides. Recently, deep learning [42] has become a promising tool to solve the inverse problem. Y. Rivenson et al [43] divided wavefield into amplitude and phase parts, and then constructed a dual-channel end-to-end network to eliminate the twin-image artifact, where clean and artifact-wrapped images form a pair for dataset training. But the performance of the learning method relies on the range of trained datasets. G. Situ et al [44] plugged a pre-defined U-net into a physical imaging model to design a self-supervised iterative network (termed as PhysenNet) for single-frame image recovery. The PhysenNet gets rid of the limitation of data dependence but only functions well for phase-only objects. Therefore, the design of single-frame imaging method remains a major challenge for achieving further improvements.

Here we propose a single-plane phase retrieval to realize high-fidelity sample reconstruction for lensfree on-chip microscopy. In our method, lensfree image recovery is constructed as a quadratic phase retrieval problem to reconstruct the transmitted field of the sample, where total variation and denoising priors are imposed to guarantee an efficient convergence. Based on the computational framework, we establish a 3D-printed lensless imaging platform to verify the superiority of our method.

2. Theory

2.1. Conventional methods

As shown in Fig. 1(a), a lensfree on-chip microscope is composed of a coherent illumination source, sample, and imaging sensor. The incident wave passes through the sample and splits into two parts: scattered wave and unscattered background. The interference of the two waves generates a hologram on the imaging sensor. Assuming the transmitted wave field of the sample is T , the resulting intensity hologram I is expressed as

$$I = |T \otimes h_Z|^2 + \varepsilon = |(R + O) \otimes h_Z|^2 + \varepsilon, \quad (1)$$

where O denotes the scattered wave passing through the sample and R is the unscattered background. h_Z is a point spread function that maps from sample to sensor plane with a diffractive distance of Z , which can be analytically denoted by a diffraction propagation kernel. \otimes represents a convolution operator. ε denotes additive noise in data acquisition. As angular spectrum model is considered, the entire definition of Eq. (1) is specified as

$$I = |\mathcal{F}^{-1}[\mathcal{F}(T)H_Z]|^2 + \varepsilon, \quad (2)$$

$$H_Z(f_x, f_y) = \begin{cases} \exp\left[\frac{2\pi jZ}{\lambda}\sqrt{1 - (\lambda f_x)^2 - (\lambda f_y)^2}\right], & (\lambda f_x)^2 + (\lambda f_y)^2 < 1 \\ 0, & (\lambda f_x)^2 + (\lambda f_y)^2 \geq 1 \end{cases} \quad (3)$$

where \mathcal{F} and \mathcal{F}^{-1} denote Fourier transform and its inverse transform. (f_x, f_y) is frequency coordinate, and λ is the wavelength of incident light. In the following context, the forward and backward operators of diffraction propagation are simplified as

$$\begin{cases} T \otimes h_Z = A_Z T = \mathcal{F}^{-1}[\mathcal{F}(T) H_Z], \\ T \otimes h_Z^* = A_Z^H T = \mathcal{F}^{-1}[\mathcal{F}(T) H_Z^*]. \end{cases} \quad (4)$$

The superscript ‘*’ denotes a complex conjugate operator. Let $U_R = A_Z R$ and $U_O = A_Z O$, Eq. (1) can be rewritten as

$$I = |A_Z R + A_Z O|^2 + \varepsilon = |U_R + U_O|^2 + \varepsilon = U_R^2 + U_O^2 + U_R^* U_O + U_R U_O^* + \varepsilon. \quad (5)$$

Assuming incident light is plane wave, the unscattered wavefield can be set as $U_R = 1$ without loss of generality. Then, Eq. (5) can be converted to

$$I = 1 + U_O^2 + U_O + U_O^* + \varepsilon. \quad (6)$$

If the hologram is de-convolved by backward propagation kernel, the back-propagated result is expressed as

$$A_Z^H I = A_Z^H 1 + A_Z^H |A_Z O|^2 + A_Z^H A_Z O + A_Z^H A_Z^H O^* + \varepsilon = A_Z^H 1 + A_Z^H |A_Z O|^2 + O + A_{2Z}^H O^* + \varepsilon. \quad (7)$$

Note that the back-propagated result consists of five parts: background constant ($A_Z^H 1$), self-interference artifact ($A_Z^H |A_Z O|^2$), object field (O), twin-image artifact ($A_{2Z}^H O^*$), and additive noise. As we find, the object information is wrapped with self-interference and twin-image artifacts. The goal of lensfree imaging is to separate the object field from other artifacts. For the compressive sensing method in Ref. [41], the quadratic and constant terms are incorporated into the noise part, and then Eq. (6) is rewritten as

$$I = U_O + U_O^* + \varepsilon = 2\text{Re}(U_O) + \varepsilon = 2\text{Re}(A_Z O) + \varepsilon. \quad (8)$$

The object field can be reconstructed by minimizing $\|2\text{Re}(A_Z O) - I\|_2^2$ by a two-step iterative shrinkage/thresholding algorithm [40]. The reconstructed accuracy of the compressive sensing method is undermined due to the missing of the quadratic term, especially for the recovery of dense samples.

Without decoupling of object and background fields, support-based phase retrieval method models lensfree image recovery as a constrained minimization problem,

$$\hat{T} = \arg \min \{ \| |A_Z T|^2 - I \|_2^2 + \mu \cdot \|T\|_{\text{sup}} \}, \quad \|T\|_{\text{sup}} = \begin{cases} T, & T \in \Omega \\ \tau, & T \notin \Omega \end{cases} \quad (9)$$

where the transmitted field T can be reconstructed by a constrained alternative projection framework between sample and sensor planes. Ω denotes the support region that can be adjusted by a shrink-wrap strategy [33–36]. τ is a background constant that is the average value of the non-support region. At the sensor plane, the amplitude is replaced by the square root of intensity measurement. At the sample plane, the information within the support region is retained and the rest is replaced by a background constant τ . However, the accurate boundary of the support

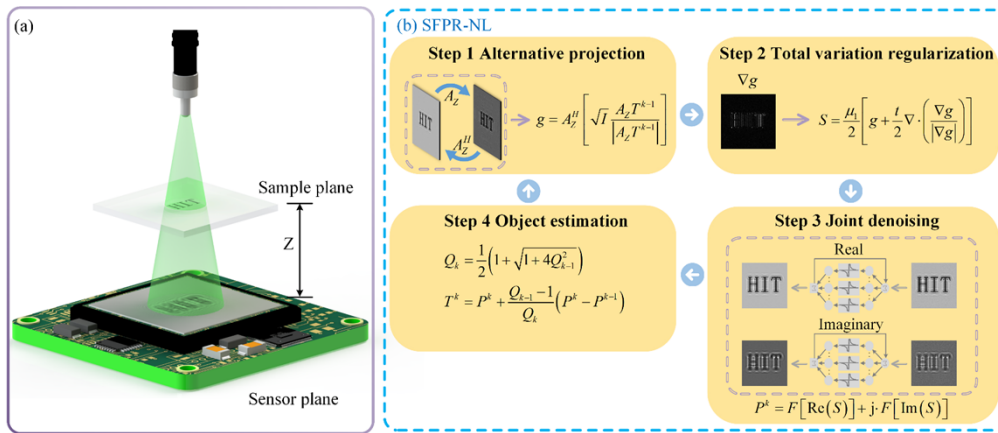


Fig. 1. Diagram of lensfree on-chip microscope and flowchart of SFPR-NL algorithm.

region cannot be sketched for dense samples. Also, replacing the background region with a constant easily filters out high-frequency information in the reconstruction. Both support-based phase retrieval and compressive sensing method are only available for sparse or isolated samples, where the self-interference term should be ignored, i.e., $U_O^2 \ll U_R^2$. However, as proved by Ozcan's team [43], this sparse assumption is difficult to be satisfied for dense samples, such as pathological slides.

Different from the above methods, deep learning provides an easy-to-use solution to map the imaging model from sample to sensor planes. As a self-supervised learning method, the PhisenNet [44] can realize a high-quality phase imaging without a large amount of data training, which constructs the following loss function and minimizes it to learn the physical imaging model R_θ

$$\hat{R}_\theta = \arg \min_{\theta \in \Theta} \|A_Z R_\theta(I) - I\|^2. \quad (10)$$

R_θ is a pre-defined U-net that maps the relationship between the phase of sample and intensity image, where a set of weights and biases $\theta \in \Theta$ can be adaptively specified by an iterative calculation. After R_θ is learned, the phase of sample can be reconstructed by using $\hat{R}_\theta(I)$. The PhisenNet releases the data dependence of deep learning and realizes a high-efficient phase recovery. But the PhisenNet is only suitable for phase-only samples and cannot handle the reconstruction of a complex wavefield.

2.2. Our method

We do not focus on the simplification of the minimization function, but model lensfree image recovery as a quadratic phase retrieval problem. To solve this ill-posed problem, we impose two prior terms and construct a complete minimization function as follows

$$\hat{T} = \arg \min \{ \| |A_Z T|^2 - I \|^2 + \mu_1 J_1(T) + \mu_2 J_2(T) \}. \quad (11)$$

Here total variation (TV) and denoising priors are designed to solve this nonlinear problem. μ_1 and μ_2 are regularization parameters ranging from 0 to 1. $J_1(T)$ is the TV term that can be expressed as, $\|T\|_{\text{TV}} = \iint |\nabla T| dx dy$, where ∇ denotes a gradient operator. The TV term introduces a gradient operation to detect edge content so that a good edge-preserving can be realized for high-frequency information [45]. The second prior $J_2(T)$ is set as denoising prior, which originates from plug-and-play optimization [46–48] and regularization of denoising [49].

The denoising prior could transfer a minimization problem into a denoising task, where a set of advanced denoisers can be exploited for different application scenarios, such as image super solution, image inpainting, or deblur. The denoising-based regularization has been applied in far-field coding diffraction imaging for noise-robustness enhancement [50–54]. Different from Refs. [50–54], the inverse problem formulated in our work is that only one hologram is recorded for image recovery and a known coding mask does not exist. Based on the dual prior setting, we solve the quadratic problem by a fast iterative shrinkage/thresholding algorithm [55] and divide the Eq. (11) into the following four steps

$$S = \arg \min_{T^{k-1}} \left\{ \left\| A_Z T^{k-1} \right\|^2 - I \right\}_2^2 + \mu_1 \| T^{k-1} \|_{\text{TV}}, \quad (12)$$

$$P^k = \arg \min_{P^{k-1}} \left\{ \| S - P^{k-1} \|_2^2 + \mu_2 J_2(P^{k-1}) \right\}, \quad (13)$$

$$Q_k = \frac{1}{2} \left(1 + \sqrt{1 + 4 Q_{k-1}^2} \right), \quad (14)$$

$$T^k = P^k + \frac{Q_{k-1} - 1}{Q_k} (P^k - P^{k-1}). \quad (15)$$

k is the index of iterations. The sub-problem in Eq. (12) can be solved by an alternative projection and gradient descent optimization as follows

$$S = \frac{\mu_1}{2} \left[g + \frac{\gamma}{2} \nabla \cdot \left(\frac{\nabla g}{|\nabla g|} \right) \right], \quad \text{s.t. } g = A_Z^H \left[\sqrt{I} \frac{A_Z T^{k-1}}{|A_Z T^{k-1}|} \right] \quad (16)$$

where γ is a step for gradient descent optimization. The explicit derivation of Eq. (16) can be found in the Supplemental document. The sub-problem in Eq. (13) can be viewed as a proximity operator of $J_2(P^{k-1})$ at point S , whose solution can be obtained by a denoising process, i.e., $P^k = F(S)$, where F denotes an image filter. Considering that the wave field is described by a complex-valued matrix, we split S into real and imaginary parts to be processed. Thus, the sub-problem in Eq. (13) is transformed into

$$P^k = F[\text{Re}(S)] + j \cdot F[\text{Im}(S)]. \quad (17)$$

We collect a set of popular denoisers, including BM3D filter [56], guided filter [57], TNRD filter [58], FFDNet [59], and recursive filter [60], to determine the optimal filter. By comparing the imaging results, TNRD filter (Trainable nonlinear reaction diffusion) is selected for this denoising task. The denoiser selection and parameter tuning are given in the Supplemental. As an end-to-end network, TNRD filter is constructed by a nonlinear reaction diffusion model, where a set of linear filters and influence functions could be parametrized and learned by minimizing the loss function. In the learning process, Gaussian noise is imposed on clear images to generate degraded images. Degraded and clear images form a pair for denoising training. Although TNRD filter is a learning-based filter, we do not train the filter with real experiment dataset but utilize a default version whose denoising model and parameters are learned from 400 natural images. Based on the above analysis, single-frame phase retrieval with nonlinear optimization is derived

as follows

$$\begin{cases} g = A_Z^H \left[\sqrt{I} \frac{A_Z T^{k-1}}{|A_Z T^{k-1}|} \right], S = \frac{\mu_1}{2} \left[g + \frac{\gamma}{2} \nabla \cdot \left(\frac{\nabla g}{|\nabla g|} \right) \right], \\ P^k = F[Re(S)] + j \cdot F[Im(S)], \\ Q_k = \frac{1}{2} \left(1 + \sqrt{1 + 4Q_{k-1}^2} \right), \\ T^k = P^k + \frac{Q_{k-1} - 1}{Q_k} (P^k - P^{k-1}). \end{cases} \quad (18)$$

In the following experiments, our method is termed as SFPR-NL (single-frame phase retrieval with nonlinear optimization) for simplicity. The parameters of SFPR-NL method are set as: $\mu_1=1$, $\gamma=0.05$, and $Q_1=0.25$. The noise variance of TNRD filter is set as 0.004. Our method only exports the transmitted field of sample. To further acquire the real object field, the background image should be additionally recorded when the sample is removed. The background image is also input to our method to reconstruct the reference field of sample R . Thus, the corresponding object field O can be extracted by $T - R$.

3. Experimental results

3.1. Experimental configuration

In experiment, we build a field-portable lensfree platform to validate the performance of our method, whose experimental configuration is displayed in Fig. 2. As shown in Fig. 2(a), a fiber-coupled incident beam with a wavelength of 532nm is modulated by pinhole and color filter (Thorlabs, FL532-1, FWHM = 1 ± 0.2 nm) to meet the requirements of spatial and temporal coherence, and then outputs a coherent wave landing on the sample. A bare CMOS sensor chip (IMX206, Sony, 4608×3456, 1.34μm) is close fixed to sample and capture the hologram of sample. The optical components and imaging sensor chip are assembled by 3D-printed modules. The sample-to-sensor distance is calibrated by an auto-focusing algorithm [61]. Figure 2(b) and Fig. 2(c) are external and internal pictures of the portable system. Figure 2(d) and Fig. 2(e) correspond to the experimental process for slide-based tissue and Petri dish. In data processing, the whole-field screen of the imaging sensor is used for image recovery and the acquired FOV amounts to 28.6mm². The current single-frame imaging methods, including support-based phase retrieval (SPR) [33], compressive sensing method (CS) [41], and PhysenNet [44], are listed as the comparison group. For a fair comparison, the parameters of SPR and CS methods are finely tuned, and their iterations are both set to 500 for good convergence. The PhysenNet is trained for two tasks, amplitude-only and phase-only nets. The amplitude-only net is applied for stained tissue and resolution target, the phase-only net is for label-free cells. The iterations and training image size of PhysenNet are 10000 and 1024×1024.

3.2. Resolution target

We utilize two resolution targets to characterize the imaging resolution for single-frame reconstruction methods. Figure 3(a1) is the captured hologram (1024×1024) for the positive resolution target (Ready Optics), the regions related to smaller line pairs are zoomed in Fig. 3(a2) and Fig. 3(a3). As the hologram is deconvolved by angular spectrum kernel, the back-propagated amplitude images are shown in Figs. 3(b1)–3(b3). It is noted from Fig. 3(b3) that the true object emerges in the back-propagated result but is wrapped with twin-image and self-interference artifacts. In Figs. 3(c1)–3(c3), the SPR method is incapable of eliminating the artifacts, and the residue error exists around the object. Especially for Fig. 3(c3), local information of Groups 8 and 9 is missing. If the support region is further shrunken, the high-frequency component will be lost. The retrieved images of CS, PhysenNet, and our method are given in Figs. 3(d)–3(f), where the noisy artifacts are removed, and clear targets are obtained. As shown in Figs. 3(d3)–3(f3), the smallest resolved targets of CS, PhysenNet and our method are element 1 of Group 8, element 6

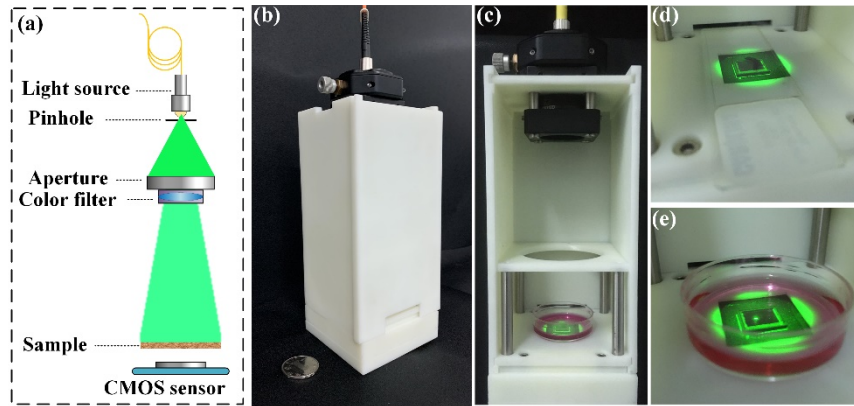


Fig. 2. Field-portable lensfree microscope used for experiment. (a) Optical configuration. (b) External view. (c) Internal view. (d) and (e) correspond to the experimental process for a slide-based sample and Petri dish.

of Group 7, and element 4 of Group 8, whose achievable half-pitch resolution is specified as $1.953\mu\text{m}$, $2.192\mu\text{m}$, and $1.381\mu\text{m}$. The resolution comparison shows that our method outperforms other methods with a higher imaging resolution. Considering that the pixel size of the sensor chip is $1.34\mu\text{m}$, the imaging resolution of our method reaches the physical limit of the present sensor chip. The computing time of SPR, CS, PhysenNet, and our method is 41s, 1854s, 1639s, and 752s, where all computation is executed on a laptop (CPU: AMD R7, RAM: 32GB, GPU: NVIDIA GeForce RTX3070).

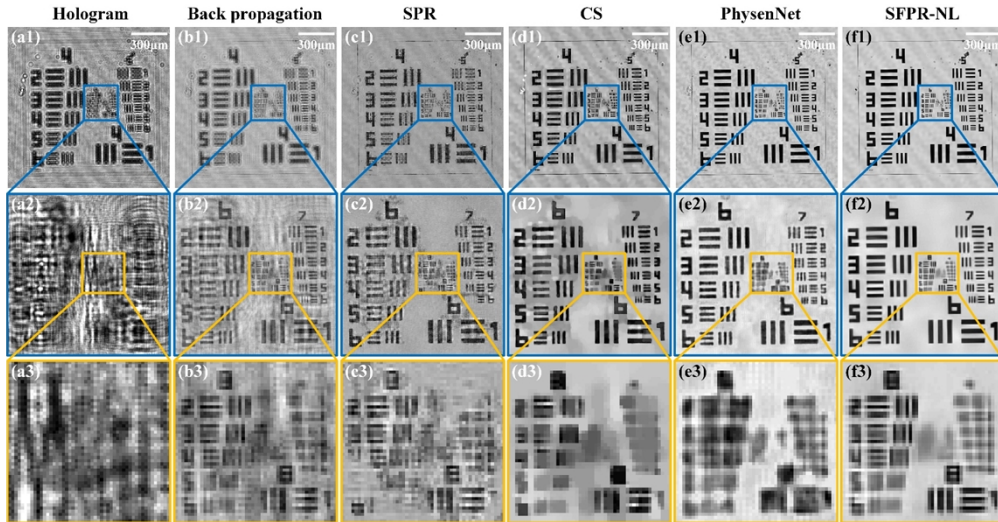


Fig. 3. Reconstructed results of positive resolution target (Ready Optics). SPR is the support-based phase retrieval [33]. CS is the compressive sensing method [41]. PhysenNet is the self-supervised learning method [44].

Figure 4 is the reconstructed amplitude images of the negative resolution target (Edmund Optics, #55-622). For the negative target, the incident wave only passes through the object region and is blocked in the background region. In this case, the captured image on the sensor is the diffraction pattern of the object, i.e. U_O^2 . Figure 4(a) is the recorded diffraction pattern of the

target, and Figs. 4(b1)–4(b3) are retrieved images by back propagation. Note that blur from diffraction is not mitigated by inverse propagation. This is because that the background field is blocked, and the holographic imaging assumption is not satisfied. The retrieved images of SPR, CS, and PhysenNet are displayed in Figs. 4(c)–4(e), where the blur is slightly alleviated, but the high-frequency content cannot be reconstructed. In contrast, our method outputs a clear image in Figs. 4(f1)–4(f3). Similar to the results of Fig. 3, the achievable half-pitch resolution of our method is still 1.381 μm. This experiment proves that our method is also feasible for coherent diffraction imaging scenario.

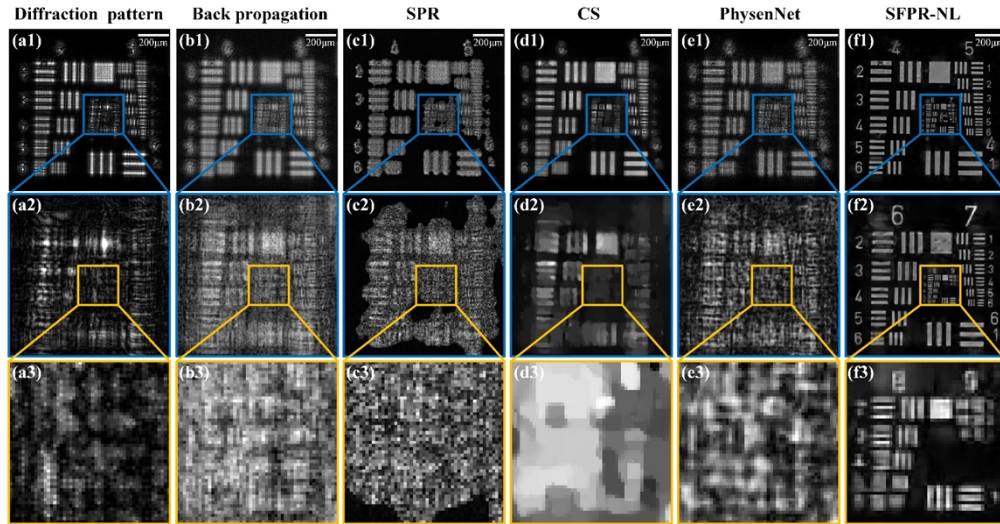


Fig. 4. Reconstructed results of negative resolution target (Edmund Optics, #55-622).

3.3. Pathological slide

The reconstructed results of H&E stained mouse lung tissue are provided in Fig. 5. Figure 5(a) is the recorded hologram, and Fig. 5(b) is the cropped region of interest for further analysis. The retrieved amplitude images of different methods are shown in Figs. 5(c)–5(g). As a reference image, an imaging result captured from a commercial wide-field microscope (Olympus, IX71, 4×/0.1) is also offered in Fig. 5(h). In Fig. 5(c), the back-propagated image can reconstruct the shape of the sample but is covered with twin-image and self-interference artifacts. The artifacts degrade the imaging quality and the texture structure of lung tissue cannot be resolved. In Fig. 5(d), the SPR method merely eliminates the background artifact, and the noise within the object region still exists. The result of the SPR method implies that the support constraint cannot separate the sample from the noisy artifacts for dense samples. In Fig. 5(e), the CS method filters out the noisy artifact at the cost of resolution loss, where the gland and cells in the bronchial tissue (labeled by red arrow) have been removed. For this lung tissue, we utilize a metric in Ref. [43] to show that the root-mean-squared (RMS) modulus ratio of the object scattered wave and background wave is 24.4%, which indicates that the sparse assumption cannot be satisfied. This is the reason why SPR and CS methods fail to realize a high-quality image recovery. As shown in Fig. 5(f), the output image of PhysenNet is distorted. This bad performance is attributed to the fact that amplitude and phase images have a strong pixel-wise mapping relationship for stained tissue. Only using an amplitude-to-intensity net is insufficient to reconstruct a complex wavefield. In Fig. 5(g), our method eliminates the noisy artifact and achieves a comparable performance with the output of the wide-field microscope (Fig. 5(h)).

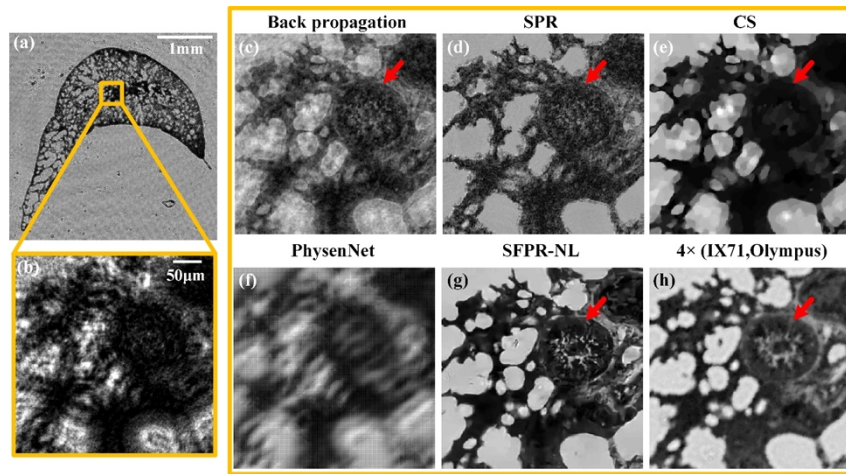


Fig. 5. Reconstructed results of H&E stained lung pathological slide.

3.4. Label-free microglia cell

The reconstruction of label-free microglia cell (BV-2) is given to verify the capability of phase imaging. The whole-field phase image is reconstructed in Fig. 6(a). The results of different methods are cropped and displayed in Figs. 6(b)–6(f). In the two regions, the cells with sparse and dense distribution are both included. The phase images of sparse cells and dense cells are retrieved in Figs. 6(b1)–6(f1) and Figs. 6(b2)–6(f2). As shown in Figs. 6(b1)–6(f1), the results of back-propagated and PhysenNet are undermined by noisy background. The other three methods remove the artifact and export contrast-enhanced phase images. For region 2, back propagation, SPR and CS methods fail to acquire a clear image. In contrast, the PhysenNet and our method accomplish phase recovery of dense cells. This result proves that our method could hold a stable phase imaging capability.

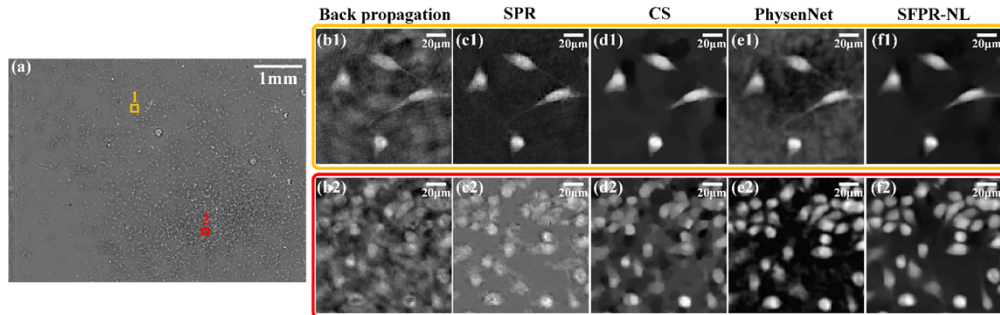


Fig. 6. Reconstructed phase images of label-free microglia cell (BV-2).

3.5. Polystyrene beads

We investigate the quantitative recovery of our method by imaging 50 μm polystyrene beads. As shown in Fig. 7, the experiment of polystyrene beads is performed to separate the object field from transmitted wavefield. When the polystyrene beads are loaded or removed, the corresponding holograms are recorded and displayed in Fig. 7(a1) and Fig. 7(a2). After these two images are input into our method, the transmitted wavefield and background wavefield can be reconstructed,

whose amplitude images are given in Fig. 7(b1) and Fig. 7(b2). Accordingly, the object field can be obtained by subtracting the background field from the transmitted field. The amplitude of the acquired object field is shown in Fig. 7(c), where a better target-to-background contrast is realized. Captured the blue cross-line from Fig. 7(c), the plotline of polystyrene beads is drawn in Fig. 7(d). It can be measured from Fig. 7(d) that the diameter of beads is $49.58\mu\text{m}$ (37 pixels $\times 1.34\mu\text{m}$), which is approximate to the ground truth value of $50\mu\text{m}$.

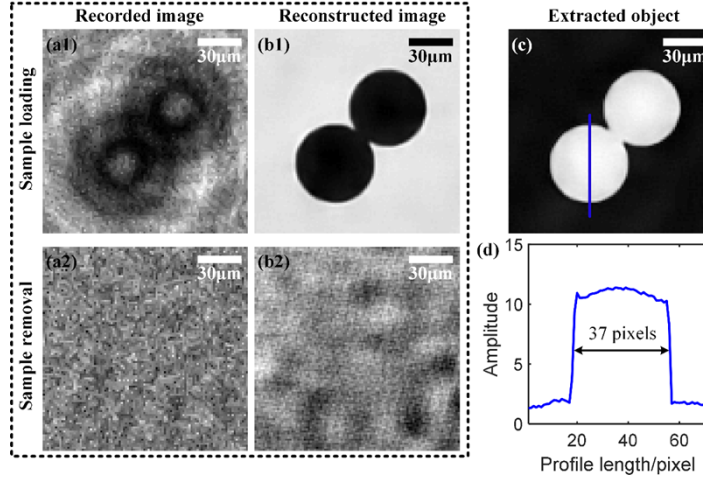


Fig. 7. Reconstructed results of polystyrene beads ($50\mu\text{m}$). (a1) and (a2) are recorded holograms when the sample is loaded or removed. (b1) and (b2) are reconstructed amplitude images that are related to the transmitted wave field and background field. (c) is obtained by subtracting the background field from the transmitted wave field. (d) is plotted from the blue cross-line of (c).

3.6. Dynamic target

As well as the above samples, dynamic targets are also employed in the portable system. In this process, we grew HeLa cell in a petri dish and placed the dish on the sensor chip for time-lapse observation. For sample preparation procedure, we only injected a small amount of cell-culture medium into the dish, which resulted in an unstable cell culture environment. In such situation, most of the cells grew adhering to the wall, but others floated above the wall. Also, insufficient nutrients could lead to cell death under long-time observation, where the morphology of dead cells shows an irregular shape. Thus, cell movement and shape change can be both observed by our method. In data acquisition, the sensor chip captures a hologram per minute, and a hologram video with 160 frames is recorded. In data processing, each frame of the hologram video is run by our method to reconstruct the phase information of HeLa cell. The retrieved image of the first frame is shown in Fig. 8(a). The regions of orange and blue boxes are cropped and zoomed for further observation. The retrieved phase images from 0 min to 12min are given in Figs. 8(b1)–8(b4). It is noted that the labelled cells move over time. Figures 8(c1)–8(c4) correspond to the phase results at the time of 0min, 54min, 107min, and 160min. In Fig. 8(c1) and Fig. 8(c2), the nutrients are enough, and the shape of the cells does not change. In Fig. 8(c3) and Fig. 8(c4), the nutrients are insufficient, and the cells start to shrink. Especially for Fig. 8(c4), the cell shrinkage is remarkable and the shape changes greatly, which implies that the cells are dead. The entire phase reconstruction results are presented as a video in supplementary material (see [Visualization 1](#)).

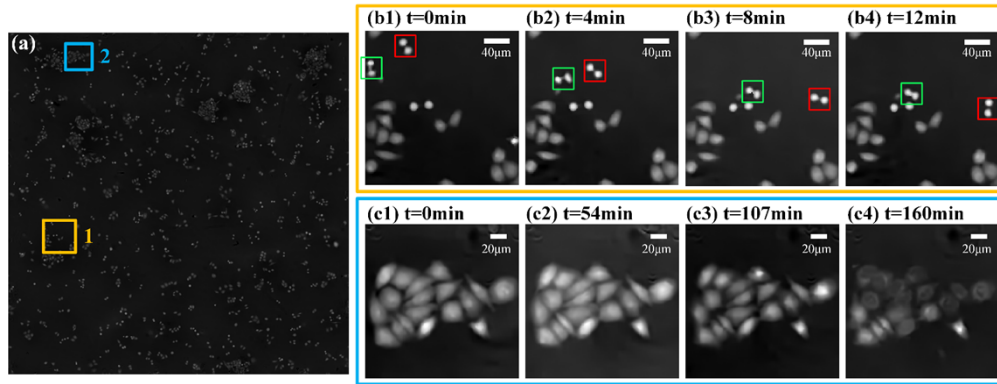


Fig. 8. Phase reconstruction of living HeLa cell from a 160min hologram video. (a) Retrieved phase image of the first frame. (b1-b4) The observation of cell movement from 0 to 12min. (c1-c4) The observation of cell death from 0 to 160min. The entire dynamic phase reconstruction results are presented as a video in [Visualization 1](#).

Another application of dynamic imaging is monitoring the microorganisms. To address this, we provide dynamic imaging results of living eelworms in Fig. 9. In the experiment, we take a drop of fresh water on a clean glass slide and inject three eelworms into the droplet. The glass slide is placed on the portable system for dynamic observation. In data acquisition, the sensor chip captures a hologram per second, and the total acquisition time amounts to 80s. From 0s to 4s, the recorded holograms are shown in Figs. 9(a1)–9(a5). As the hologram video is processed frame by frame, the reconstructed amplitude and phase images of the eelworm are displayed in Figs. 9(b1)–9(b5) and Figs. 9(c1)–9(c5), respectively. The entire raw data and reconstructed results can be found in [Visualization 2](#). The experiments of dynamic targets demonstrate that our method has the ability of time-lapse imaging.

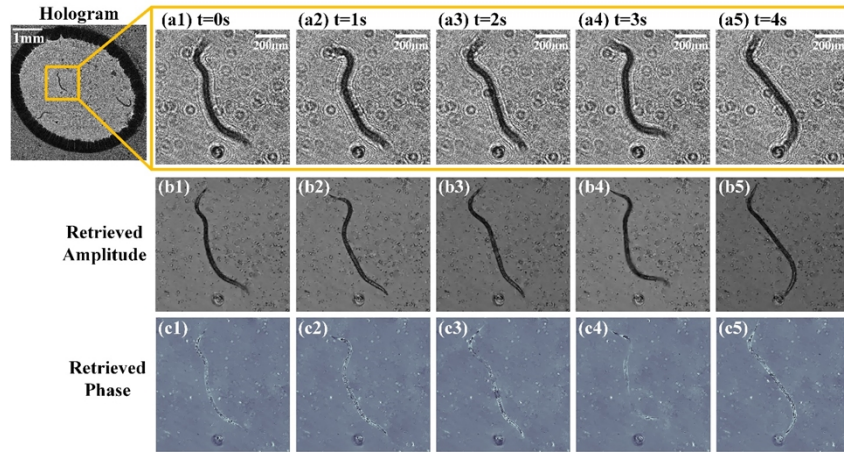


Fig. 9. Reconstructed results of living eelworms from an 80s hologram video. (a1-a5) Recorded holograms from 0 to 4s. (b1-b5) and (c1-c5) are reconstructed amplitude and phase images for (a1-a5). The entire reconstructed results are presented as a video in [Visualization 2](#).

3.7. Pixel super resolved imaging

We expand our method to pixel super-resolved (PSR) imaging. The resolution of the lensless on-chip system is limited by the pixelation of imaging sensor. To break the limitation, a typical strategy is to translate the hologram with sub-pixel shifts and fuse the shifted holograms by pixel super resolution algorithm to acquire a PSR hologram. we follow the strategy in Ref. [62] and install the pinhole on a 2D translation stage for multi-angle illumination. After the pinhole is laterally moved, multiple holograms with subpixel shifts can be recorded. Accordingly, 25 raw holograms are captured under different illuminating angles, where the corresponding subpixel shifts are precisely evaluated by image registration algorithm. Using a raw hologram, SFPR-NL algorithm reconstructs a low-resolution result in Fig. 10(a). As the hologram is interpolated with an unsampled factor of 2, the retrieved result using the interpolated hologram is given in Fig. 10(b). The comparison of Fig. 10(a) and Fig. 10(b) indicates that the interpolation of the hologram could increase the half-pitch resolution from $1.38\mu\text{m}$ to $1.096\mu\text{m}$, but it cannot realize a sub-micron resolution. By running the PSR algorithm [63], 25 raw holograms are fused into a PSR hologram. Using the PSR data, our method reconstructs the resolution target in Fig. 10(c). It is noted that the resolved smallest target is element 4 of Group 9 and the achievable half-pitch resolution is 691 nm, which surpasses the pixel limitation and reaches the sub-pixel resolution. The PSR reconstruction of stained intestinal submucosa is offered in Fig. 11. Figure 11(a) and Fig. 11(b) are reconstructed by SFPR-NL method using raw and PSR hologram. In comparison with Fig. 11(a), the detailed information of intestinal submucosa is remarkably enhanced in Fig. 11(b). The radially-averaged spatial frequency spectrum (RASF) [64] is also employed for a quantitative characterization. The logarithmic RASF curves of Fig. 11(a) and Fig. 11(b) are plotted in Fig. 11(c). It is noted that the RASF values of Fig. 11(b) are larger than that of Fig. 11(a), which accords with the visual judgment, i.e., the resolution of lensfree image recovery is strengthened by enforcing pixel super resolution. The PSR experiments prove that our method is compatible with the PSR hologram. Also, compared to the multi-height or multi-wavelength PSR strategy, our method only needs a single-plane dataset, which enables a data-efficient reconstruction.

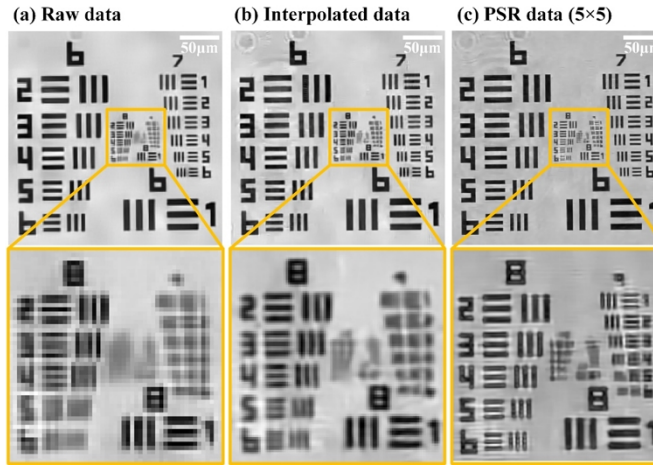


Fig. 10. Pixel super resolved reconstruction of the resolution target. (a-c) are reconstructed targets by using raw hologram, interpolated hologram, and pixel super-resolved hologram.

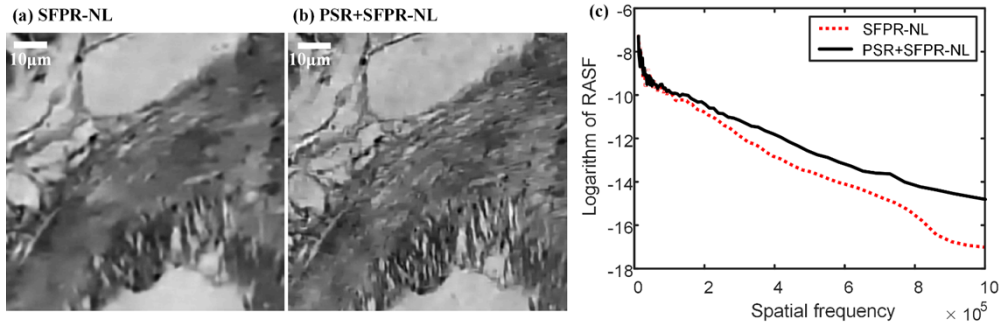


Fig. 11. Pixel super resolved reconstruction of stained intestine tissue. (a) and (b) are reconstructed images using raw hologram and super-resolved hologram. (c) The logarithmic radially-averaged spatial frequency spectrum of (a) and (b).

3.8. Quantitative evaluation of reconstructed accuracy

We conduct an extra experiment in a lensfree multi-height configuration to indicate the reconstructed accuracy of our method. In the multi-height system, the imaging sensor is installed on a motorized stage and 11 holograms of a stained breast tissue slide are captured with different sample-to-sensor distances. All defocused holograms are input to multi-height phase retrieval [18–22] to reconstruct the ground truth image. For single-frame imaging methods, only one hologram at the first height is used for image recovery. The structural similarity index measure (SSIM) [65] of the single-frame reconstructed image and ground truth is employed as a quantitative indicator of reconstructed accuracy. The SSIM metric ranges from 0 to 1, and a bigger SSIM

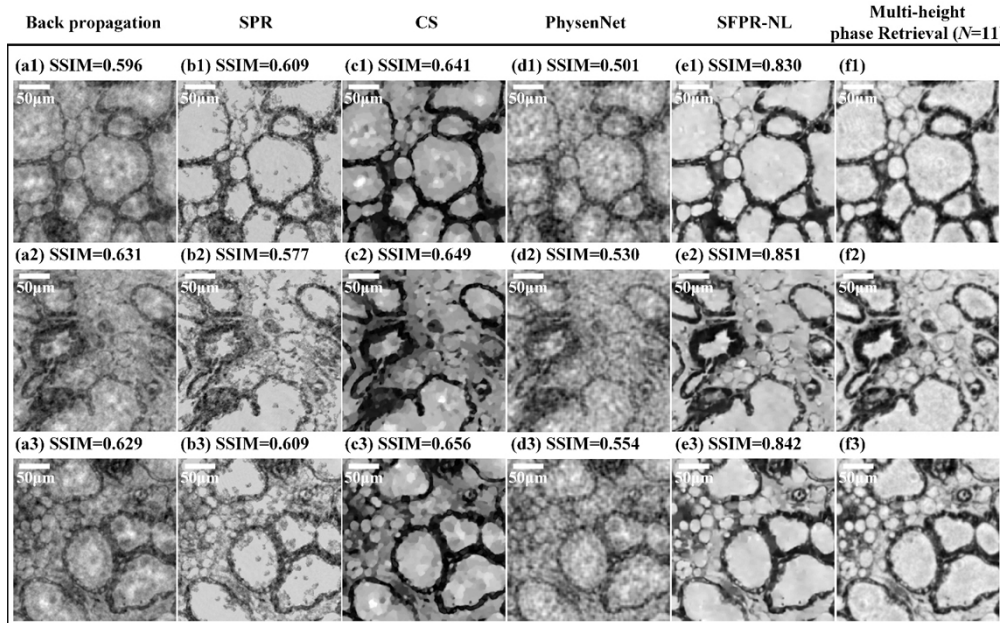


Fig. 12. Comparison of reconstructed accuracy for different single-frame imaging methods. (f1-f3) are ground truth images retrieved by multi-height phase retrieval using 11 holograms. The SSIM values between (a-e) and ground truth images are calculated and labeled.

value represents higher accuracy of image reconstruction. The reconstructed amplitude images of H&E stained breast tissue are given in Fig. 12, where the area size of cropped regions is $268\mu\text{m} \times 268\mu\text{m}$. Figures 12(f1)–12(f3) are ground truth images retrieved by multi-height phase retrieval using 11 holograms. As the hologram at the first height is fed to single-frame imaging methods, the results of back propagation, SPR, CS, PhysenNet, and our method are shown in Figs. 12(a)–12(e), and the corresponding SSIM values are also labeled. It is noted that the acquired SSIM values of our method are ~ 0.8 , while the SSIM values of other methods are ~ 0.6 . The SSIM comparison accords with the visual judgment, which indicates that the reconstructed accuracy of our method is superior to other methods. As the region with a size of 1024×1024 is selected for image recovery, the computing time of SPR, CS, PhysenNet, and our method is 42s, 1945s, 1643s, and 775s for this stained breast tissue. Using 11 holograms, the running time of multi-height phase retrieval is 47s. Compared to multi-height phase retrieval, our method spends more time on calculation but unfreezes the limitation of multi-frame measurement. The comparison results of another stained sample are presented in the Supplemental document.

4. Conclusions

In summary, we have proposed a high-fidelity lensfree imaging method to eliminate the twin-image and self-interference artifacts using only one hologram intensity. To this end, we first construct the lensfree image recovery as a nonlinear phase retrieval problem, and then solve it by a fast iterative shrinkage/thresholding algorithm, where total variation and denoising priors are imposed to guarantee an efficient convergence. Experimental results of different samples show that the proposed method can achieve a high-fidelity image recovery and outperform the state-of-the-art methods with higher reconstruction accuracy. Compared to the end-to-end learning method [43], our method avoids collecting a large number of experimental datasets for training. The running time of our method is constrained by TNRD filter, in which an image should be cropped to a series of patches to be processed. To improve it, a parallel calculation can be executed to accelerate the patch process of TNRD filter. Our method not only decreases the data amount down to a single-frame but also realizes a high-fidelity image reconstruction, which contributes a data-efficient, simple, and robust computational framework to design a low-cost and resource-limited lensless microscope.

Funding. National Natural Science Foundation of China (51775148, 61975044).

Disclosures. The authors declare no conflicts of interest.

Data Availability. Data and code underlying the results presented in this paper are not publicly available at this time but may be obtained from Dr. Cheng Guo upon reasonable request.

Supplemental document. See [Supplement 1](#), [Visualization 1](#), and [Visualization 2](#) for supporting content.

References

1. A. Greenbaum, W. Luo, T. Su, Z. Göröcs, L. Xue, S. O. Isikman, A. F. Coskun, O. Mudanyali, and A. Ozcan, "Imaging without lenses: achievements and remaining challenges of wide-field on-chip microscopy," *Nat. Methods* **9**(9), 889–895 (2012).
2. G. Zheng, S. A. Lee, Y. Antebi, M. B. Elowitz, and C. Yang, "The ePetri dish, an on-chip cell imaging platform based on subpixel perspective sweeping microscopy (SPSM)," *Proc. Natl. Acad. Sci. U. S. A.* **108**(41), 16889–16894 (2011).
3. G. Kuo, F. Liu, I. Grossrubatscher, R. Ng, and L. Waller, "On-chip fluorescence microscopy with a random microlens diffuser," *Opt. Express* **28**(6), 8384–8399 (2020).
4. A. Greenbaum, Y. Zhang, A. Feizi, P. Chung, W. Luo, S. R. Kandukuri, and A. Ozcan, "Wide-field computational imaging of pathology slides using lensfree on-chip microscopy," *Sci. Transl. Med.* **6**(267), 267ra175 (2014).
5. P. Song, R. Wang, J. Zhu, T. Wang, Z. Bian, Z. Zhang, K. Hoshino, M. Murphy, S. Jiang, C. Guo, and G. Zheng, "Super-resolved multispectral lensless microscopy via angletilted, wavelength-multiplexed ptychographic modulation," *Opt. Lett.* **45**(13), 3486–3489 (2020).
6. W. Bishara, H. Zhu, and A. Ozcan, "Holographic opto-fluidic microscopy," *Opt. Express* **18**(26), 27499–27510 (2010).

7. G. Zheng, S. A. Lee, S. Yang, and C. Yang, "Sub-pixel resolving optofluidic microscope for on-chip cell imaging," *Lab Chip* **10**(22), 3125–3129 (2010).
8. Y. Wu, A. Shiledar, Y. Li, J. Wong, S. Feng, X. Chen, C. Chen, K. Jin, S. Janamian, Z. Yang, Z. S. Ballard, Z. Göröcs, A. Feizi, and A. Ozcan, "Air quality monitoring using mobile microscopy and machine learning," *Light: Sci. Appl.* **6**(9), e17046 (2017).
9. L. Herve, O. Cioni, P. Blandin, F. Navarro, M. Menneteau, T. Bordy, S. Morales, and C. Allier, "Multispectral total-variation reconstruction applied to lens-free microscopy," *Biomed. Opt. Express* **9**(11), 5828–5836 (2018).
10. S. A. Lee, G. Zheng, N. Mukherjee, and C. Yang, "On-chip continuous monitoring of motile microorganisms on an ePetri platform," *Lab Chip* **12**(13), 2385–2390 (2012).
11. D. Gabor, "A new microscopic principle," *Nature* **161**(4098), 777–778 (1948).
12. J. W. Goodman and R. W. Lawrence, "Digital image formation from electronically detected holograms," *Appl. Phys. Lett.* **11**(3), 77–79 (1967).
13. M. Sanz, J. A. Picazo-Bueno, J. García, and V. Micó, "Dual-mode holographic microscopy imaging platform," *Lab Chip* **18**(7), 1105–1112 (2018).
14. M. Sanz, J. A. Picazo-Bueno, J. García, and V. Micó, "Improved quantitative phase imaging in lensless microscopy by single-shot multi-wavelength illumination using a fast convergence algorithm," *Opt. Express* **23**(16), 21352–21365 (2015).
15. W. Luo, Y. Zhang, A. Feizi, Z. Gorocs, and A. Ozcan, "Pixel super-resolution using wavelength scanning," *Light: Sci. Appl.* **5**(4), e16060 (2016).
16. W. Luo, A. Greenbaum, Y. Zhang, and A. Ozcan, "Synthetic aperture-based on-chip microscopy," *Light: Sci. Appl.* **4**(3), e261 (2015).
17. Y. Zhou, J. Wu, J. Suo, X. Han, G. Zheng, and Q. Dai, "Single-shot lensless imaging via simultaneous multi-angle LED illumination," *Opt. Express* **26**(17), 21418–21432 (2018).
18. G. Pedrini, W. Osten, and Y. Zhang, "Wave-front reconstruction from a sequence of interferograms recorded at different planes," *Opt. Lett.* **30**(8), 833–835 (2005).
19. A. Greenbaum and A. Ozcan, "Maskless imaging of dense samples using pixel super-resolution based multi-height lensfree on-chip microscopy," *Opt. Express* **20**(3), 3129–3143 (2012).
20. Y. Zhang, Y. Shin, K. Sung, S. Yang, H. Chen, H. Wang, D. Teng, Y. Rivenson, R. P. Kulkarni, and A. Ozcan, "3D imaging of optically cleared tissue using a simplified CLARITY method and on-chip microscopy," *Sci. Adv.* **3**(8), e1700553 (2017).
21. C. Guo, X. Liu, X. Kan, F. Zhang, J. Tan, S. Liu, and Z. Liu, "Lensfree on-chip microscopy based on dual-plane phase retrieval," *Opt. Express* **27**(24), 35216–35229 (2019).
22. Y. Rivenson, Y. Wu, H. Wang, Y. Zhang, A. Feizi, and A. Ozcan, "Sparsity-based multi-height phase recovery in holographic microscopy," *Sci. Rep.* **6**(1), 37862 (2016).
23. V. Katkovnik, I. Shevkunov, N. V. Petrov, and K. Egiazarian, "Computational super-resolution phase retrieval from multiple phase-coded diffraction patterns: simulation study and experiments," *Optica* **4**(7), 786–794 (2017).
24. Y. Wu, M. K. Sharma, and A. Veeraraghavan, "WISH: wavefront imaging sensor with high resolution," *Light: Sci. Appl.* **8**(1), 44 (2019).
25. M. Lee, O. Yaglidere, and A. Ozcan, "Field-portable reflection and transmission microscopy based on lensless holography," *Opt. Express* **2**(9), 2721–2730 (2011).
26. S. Jiang, J. Zhu, P. Song, C. Guo, Z. Bian, R. Wang, Y. Huang, S. Wang, H. Zhang, and G. Zheng, "Wide-field, high-resolution lensless on-chip microscopy via near-field blind ptychographic modulation," *Lab Chip* **20**(6), 1058–1065 (2020).
27. H. Zhang, Z. Bian, S. Jiang, J. Liu, P. Song, and G. Zheng, "Field-portable quantitative lensless microscopy based on translated speckle illumination and sub-sampled ptychographic phase retrieval," *Opt. Lett.* **44**(8), 1976–1979 (2019).
28. T. Latychevskaia and H.-W. Fink, "Solution to the Twin Image Problem in Holography," *Phys. Rev. Lett.* **98**(23), 233901 (2007).
29. R. Corman, W. Boutou, A. Campalans, P. Radicella, J. Duarte, M. Khodoltsova, L. Ballycuif, N. Dray, F. Harms, G. Dovillaire, S. Bucourt, and H. Merjdi, "Lensless microscopy platform for single cell and tissue visualization," *Biomed. Opt. Express* **11**(5), 2806–2817 (2020).
30. C. Gaur, B. Mohan, and K. Khare, "Sparsity-assisted solution to the twin image problem in phase retrieval," *J. Opt. Soc. Am. A* **32**(11), 1922–1927 (2015).
31. J. Song, C. L. Swisher, H. Im, S. Jeong, D. Pathania, Y. Iwamoto, M. Pivovarov, R. Weissleder, and H. Lee, "Sparsity-Based Pixel Super Resolution for Lens-Free Digital Inline Holography," *Sci. Rep.* **6**(1), 24681 (2016).
32. Z. Li, Q. Yan, Y. Qin, W. Kong, G. Li, M. Zou, D. Wang, Z. You, and X. Zhou, "Sparsitybased continuous wave terahertz lens-free on-chip holography with subwavelength resolution," *Opt. Express* **27**(2), 702–713 (2019).
33. O. Mudanyali, D. Tseng, C. Oh, S. O. Isikman, I. Sencan, W. Bishara, C. Oztoprak, S. Seo, B. Khademhosseini, and A. Ozcan, "Compact, light-weight and cost-effective microscope based on lensless incoherent holography for telemedicine applications," *Lab Chip* **10**(11), 1417–1428 (2010).
34. A. Jesacher, W. Harm, S. Bernet, and M. Ritsch-Marte, "Quantitative single-shot imaging of complex objects using phase retrieval with a designed periphery," *Opt. Express* **20**(5), 5470–5480 (2012).
35. D. Ryu, Z. Wang, K. He, G. Zheng, R. Horstmeyer, and O. Cossairt, "Subsampled phase retrieval for temporal resolution enhancement in lensless on-chip holographic video," *Biomed. Opt. Express* **8**(3), 1981–1995 (2017).

36. S. M. F. Raupach, "Cascaded adaptive-mask algorithm for twin-image removal and its application to digital holograms of ice crystals," *Appl. Opt.* **48**(2), 287–301 (2009).
37. R. Horisaki, Y. Ogura, M. Aino, and J. Tanida, "Single-shot phase imaging with a coded aperture," *Opt. Lett.* **39**(22), 6466–6469 (2014).
38. R. Horisaki, R. Egami, and J. Tanida, "Experimental demonstration of single-shot phase imaging with a coded aperture," *Opt. Express* **23**(22), 28691–28697 (2015).
39. R. W. Gerchberg and W. O. Saxton, "A practical algorithm for the determination of phase from image and diffraction plane pictures," *Optik* **35**(2), 237–246 (1972).
40. J. M. Bioucas-Dias and M. A. T. Figueiredo, "A new TwIST: two-step iterative shrinkage/thresholding algorithms for image restoration," *IEEE Trans. Image Process.* **16**(12), 2992–3004 (2007).
41. W. Zhang, L. Cao, D. J. Brady, H. Zhang, J. Cang, H. Zhang, and G. Jin, "Twin-image-free holography: a compressive sensing approach," *Phys. Rev. Lett.* **121**(9), 093902 (2018).
42. G. Barbastathis, A. Ozcan, and G. Situ, "On the use of deep learning for computational imaging," *Optica* **6**(8), 921–943 (2019).
43. Y. Rivenson, Y. Zhang, H. Günaydin, D. Teng, and A. Ozcan, "Phase recovery and holographic image reconstruction using deep learning in neural networks," *Light: Sci. Appl.* **7**(2), 17141 (2018).
44. F. Wang, Y. Bian, H. Wang, M. Lyu, G. Pedrini, W. Osten, G. Barbastathis, and G. Situ, "Phase imaging with an untrained neural network," *Light: Sci. Appl.* **9**(1), 77 (2020).
45. A. Chambolle, "An Algorithm for Total Variation Minimization and Applications," *J. Math. Imaging Vis.* **20**(1/2), 163–177 (2004).
46. S. Boyd, N. Parikh, E. Chu, B. Peleato, and J. Eckstein, "Distributed optimization and statistical learning via the alternating direction method of multipliers," *Found. Trends Machine Learn.* **3**(1), 1–122 (2010).
47. A. Rond, R. Giry, and M. Elad, "Poisson inverse problems by the plug-and-play scheme," *J. Vis. Commun. Image Recogn.* **41**, 96–108 (2016).
48. U. S. Kamilov, H. Mansour, and B. Wohlberg, "A plug-and-play priors approach for solving nonlinear imaging inverse problems," *IEEE Signal Proc. Lett.* **24**(12), 1872–1876 (2017).
49. Y. Romano, M. Elad, and P. Milanfar, "The Little Engine That Could: Regularization by Denoising (RED)," *SIAM J. Imaging Sci.* **10**(4), 1804–1844 (2017).
50. B. Shi, Q. Lian, X. Huang, and N. An, "Constrained phase retrieval: when alternating projection meets regularization," *J. Opt. Soc. Am. B* **35**(6), 1271–1281 (2018).
51. C. Metzler, P. Schniter, A. Veeraraghavan, and R. G. Baraniuk, "prDeep: robust phase retrieval with a flexible deep network," in *Proceedings of International Conference on Machine Learning (ICML, 2018)*, pp. 3501–3510.
52. B. Shi, Q. Lian, and X. Fan, "PPR: Plug-and-play regularization model for solving nonlinear imaging inverse problems," *Signal Process.* **162**, 83–96 (2019).
53. B. Shi, Q. Lian, and H. Chang, "Deep prior-based sparse representation model for diffraction imaging: A plug-and-play method," *Signal Process.* **168**, 107350 (2020).
54. X. Chang, L. Bian, and J. Zhang, "Large-scale phase retrieval," *eLight* **1**(1), 4 (2021).
55. A. Beck and M. Teboulle, "A fast iterative shrinkage-thresholding algorithm for linear inverse problems," *SIAM J. Imaging Sci.* **2**(1), 183–202 (2009).
56. K. Dabov, A. Foi, V. Katkovnik, and K. Egiazarian, "Image denoising by sparse 3-d transform-domain collaborative filtering," *IEEE Trans. Image Process.* **16**(8), 2080–2095 (2007).
57. K. He, J. Sun, and X. Tang, "Guided image filtering," *IEEE Trans. Pattern Anal.* **35**(6), 1397–1409 (2013).
58. Y. Chen and T. Pock, "Trainable nonlinear reaction diffusion: a flexible framework for fast and effective image restoration," *IEEE Trans. Pattern Anal.* **39**(6), 1256–1272 (2017).
59. K. Zhang, W. Zuo, and L. Zhang, "FFDNet: toward a fast and flexible solution for CNN based image denoising," *IEEE Trans. Image Process.* **27**(9), 4608–4622 (2018).
60. Y. Chi and S. H. Chan, "Fast and Robust Recursive Filter for Image Denoising," in *Proceedings of IEEE International Conference on Acoustics, Speech and Signal Processing (IEEE, 2018)*, pp. 1708–1712.
61. Y. S. Choi and S. J. Lee, "Three-dimensional volumetric measurement of red blood cell motion using digital holographic microscopy," *Appl. Opt.* **48**(16), 2983–2990 (2009).
62. W. Bishara, T. Su, A. F. Coskun, and A. Ozcan, "Lensfree on-chip microscopy over a wide field-of-view using pixel super-resolution," *Opt. Express* **18**(11), 11181–11191 (2010).
63. R. Hardie, "A Fast image super-resolution algorithm using an adaptive Wiener filter," *IEEE Trans. Image Process.* **16**(12), 2953–2964 (2007).
64. T. Liu, K. Haan, Y. Rivenson, Z. Wei, X. Zeng, Y. Zhang, and A. Ozcan, "Deep learning-based superresolution in coherent imaging systems," *Sci. Rep.* **9**(1), 3926 (2019).
65. Z. Wang, A. C. Bovik, H. R. Sheikh, and E. P. Simoncelli, "Image quality assessment: from error visibility to structural similarity," *IEEE Trans. Image Process.* **13**(4), 600–612 (2004).